

# Aiming Strategy for a Circular Aperture Receiver: Experimental Validation at PROTEAS

Alberto Sánchez-González<sup>1</sup>[\[https://orcid.org/0000-0002-9833-592X\]](https://orcid.org/0000-0002-9833-592X), Derwalt J. Erasmus<sup>2</sup>[\[https://orcid.org/0000-0002-1642-9480\]](https://orcid.org/0000-0002-1642-9480), and Marios C. Georgiou<sup>3</sup>[\[https://orcid.org/0000-0002-4612-1188\]](https://orcid.org/0000-0002-4612-1188)

<sup>1</sup> Universidad Carlos III de Madrid, Spain

<sup>2</sup> Stellenbosch University, South Africa

<sup>3</sup> The Cyprus Institute, Cyprus

**Abstract.** An aiming strategy is developed for a circular aperture receiver at the PROTEAS field in Cyprus. To reduce thermal stress, a uniform flux distribution is searched by minimizing the coefficient of variation and the spillage losses. The combination of  $k=0.9$  and  $damp=0.85$  produces the optimal flux distribution, at the expense of increasing the spillage losses by 21.8 percentage points. To validate the model, heliostat images were utilized to synthetically generate experimental flux maps, both for single and optimized aiming. As a result, the peak flux concentration is decreased from 1090 (single-point aiming) to 367 suns with the uniform distribution.

**Keywords:** Heliostat Field, Aim Point, Uniform Flux Distribution, Spillage

## 1. Introduction

Solar central receivers have limitations in thermal stress and fatigue. Single aiming (all heliostats aim at a single point) leads to a large peak flux and sharp gradients, which may permanently damage the receiver. Uniform flux distributions are required to reduce the thermal stresses [1].

Aiming strategies must be developed and implemented to avoid such issues. On one hand, metaheuristic methods have been applied for flat plate [2] and cavity [3] receivers. On the other hand, specific algorithms have been proposed, such as the image size priority [4] and the aiming factor approach [5], which are respectively implemented in SolarPILOT [6] and FluxSPT [7].

These aiming strategies must be developed also for circular aperture receivers. The aiming factor approach has been recently adapted for circular receivers, this implementation has been called Blossaim [8]. This paper presents the implementation and the validation of the Blossaim strategy on the PROTEAS facility [9,10].

## 2. Experimental campaign at PROTEAS

The Platform for Research, Observation and Technological Applications in Solar Energy (PROTEAS) is the most complete research and development facility in Cyprus [10]. The solar tower plant (Fig. 1, left) consists of a field of 50 heliostats and an 18-meter-tall tower. The solar receiver, named iSTORE, has a circular aperture of 0.8 m in diameter. On the tower, 2.45 m above the receiver, a 2x2 m<sup>2</sup> white diffusive (Lambertian) target is utilized by the

beam characterization system. Both receiver and target are tilted  $10^\circ$  with respect to the vertical plane. The beam characterization system consists of a digital CCD camera with appropriate filters, that takes a grayscale picture of the Lambertian target and so determines the flux image by the image processing technique described in Section 3.

Heliostats consists of a single  $5 \text{ m}^2$  square mirror and follow spinning-elevation tracking. The heliostat field is arranged in 5 rows labeled from A to E, as shown in the layout in Fig. 1 (right). In each row, heliostats are subsequently numbered, with "1" being the most western one. Row A consists of 9 heliostats, 8 in last row E, while rows B, C and D contain 11 heliostats each. In total, the PROTEAS field encompasses 50 heliostats. Except for a couple of exceptions, the focal length of the mirrors is 25 m in the first two rows, 33 m in rows C and D and 45 m in the last row.

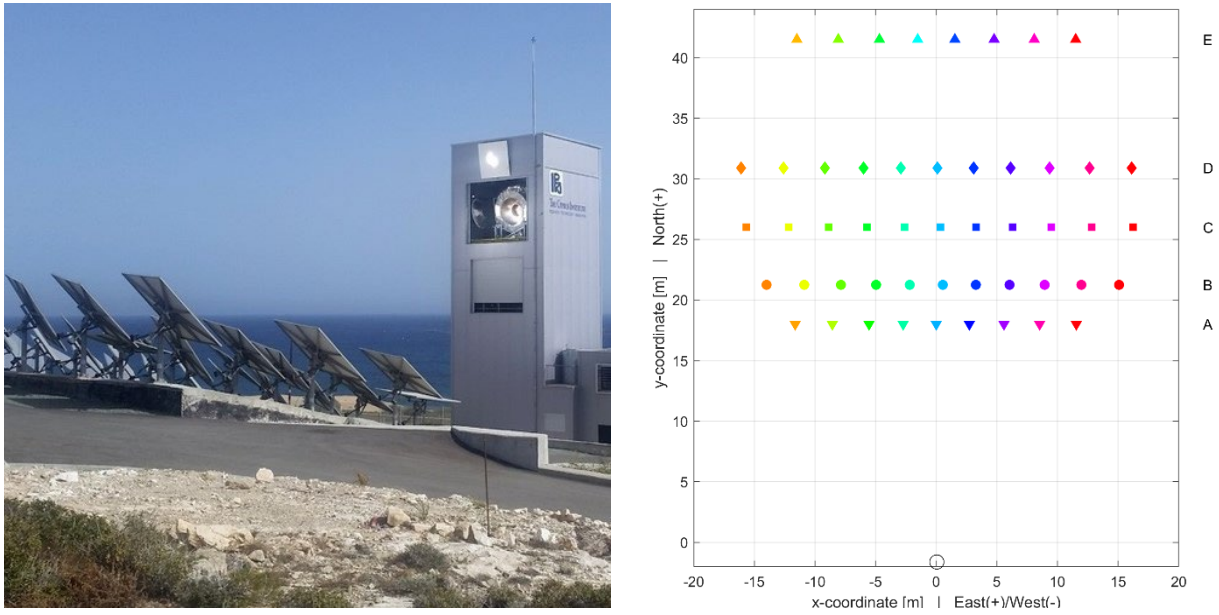


**Figure 1.** View of PROTEAS heliostat field and central tower with iSTORE receiver (left), and field layout with heliostats identified by symbol and color (right).

At the moment of the experimental campaign, the moving cooled target in front of the iSTORE was not ready. Therefore, experimental flux maps with all the heliostats simultaneously aiming at the receiver could not be taken. Alternatively, the image of every single heliostat on the Lambertian target was acquired in a short enough period. By superimposing the heliostat images by each heliostat, synthetically generated experimental flux maps can be generated, as described in Section 5.

The image acquisition was performed on the 27<sup>th</sup> of January 2022. Between 14:15 and 15:45, local time, one after another each heliostat was subsequently aimed at the target and its image was recorded. Four heliostats (B8, C1, C7 and D1) were not operational on the day of the acquisition, so that the image of their next heliostat (B9, C2, C8 and D2) was utilized.

### 3. Image processing

The acquired heliostat images provide relative irradiance levels, which are converted into a normalized ratio (from 0 to 1) by dividing each pixel level by the maximum one. The resulting images are equivalent to the normalized concentration ratio of flux density ( $C_N$ ), that is the ratio between the local flux density ( $F$ ) and the maximum one ( $F_{max}$ ),

$$C_N = \frac{F}{F_{max}} \quad (1)$$

Using a flux mapping model, additional experimental data can be estimated for each heliostat: the mirror slope error and the (absolute) concentration ratio of flux density.

### 3.1. Slope error

According to the manufacturer, the surface slope error (SSE) of the heliostats might be in the range between 0.7 and 2.5 mrad. For the mirrors currently installed at PROTEAS, there is no measurement of the slope error. This parameter can be estimated by comparison with the flux maps generated by a model. In this instance, FluxSPT has been utilized, which takes advantage of the convolution-projection model [7].

A fitting process is performed so that the slope error is varied in the model. The optimal SSE is found when the cross-correlation coefficient (CCC) between the experimental and the model is maximum. For heliostats B10 and D2, Figure 2 shows the contours of normalized concentration ratio both experimentally (dashed contours) and modeled (solid). On the background the grayscale experimental image is also shown.

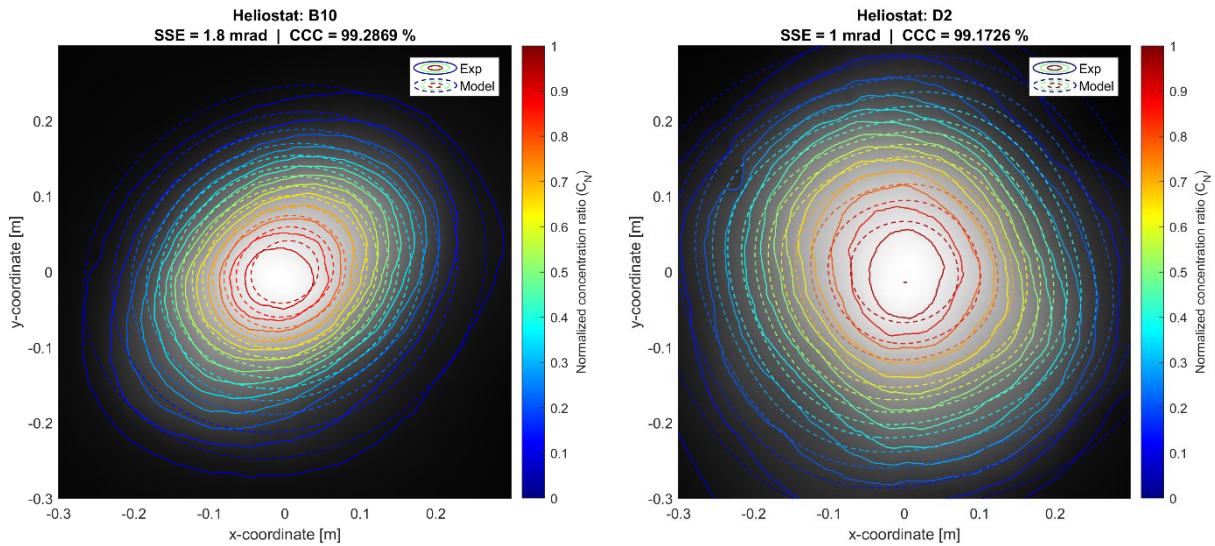


**Figure 2.** Experimental (grayscale and dotted lines) vs. model fitting the surface slope error (solid lines) for heliostats B10 (left) and D2 (right).  
Contours of normalized concentration ratio at the Lambertian target.

This fitting process is performed for all the heliostats in the PROTEAS field, reaching an average CCC of 94%. The lowest CCCs, around 80%, correspond to the heliostats in the first row, with larger astigmatism. The resulting SSE are displayed in Table 1, which range between 1.0 and 4.0 mrad. These results are in agreement with the manufacturer specifications that stated that the mirrors with shorter focal lengths have larger slope errors.

**Table 1.** Fitted surface slope errors (SSE) for PROTEAS heliostats.

| Hel. Row A | SSE [mrad] | Hel. Row B | SSE [mrad] | Hel. Row C | SSE [mrad] | Hel. Row D | SSE [mrad] | Hel. Row E | SSE [mrad] |
|------------|------------|------------|------------|------------|------------|------------|------------|------------|------------|
| A1         | 3.2        | B1         | 1.0        | C1         | as C2      | D1         | as D2      | E1         | 1.5        |
| A2         | 2.3        | B2         | 3.1        | C2         | 1.3        | D2         | 1.0        | E2         | 1.3        |
| A3         | 2.1        | B3         | 1.9        | C3         | 2.2        | D3         | 2.1        | E3         | 1.7        |
| A4         | 3.6        | B4         | 1.9        | C4         | 2.5        | D4         | 1.1        | E4         | 1.7        |
| A5         | 3.5        | B5         | 2.4        | C5         | 2.1        | D5         | 1.5        | E5         | 1.3        |
| A6         | 1.5        | B6         | 1.7        | C6         | 2.5        | D6         | 1.7        | E6         | 1.4        |
| A7         | 3.9        | B7         | 2.8        | C7         | as C8      | D7         | 1.7        | E7         | 1.3        |
| A8         | 4.0        | B8         | as B9      | C8         | 2.5        | D8         | 1.7        | E8         | 1.6        |

|    |     |     |     |     |     |     |     |  |  |
|----|-----|-----|-----|-----|-----|-----|-----|--|--|
| A9 | 2.6 | B9  | 2.1 | C9  | 2.3 | D9  | 1.5 |  |  |
|    |     | B10 | 1.8 | C10 | 1.8 | D10 | 1.7 |  |  |
|    |     | B11 | 2.8 | C11 | 1.6 | D11 | 1.6 |  |  |

### 3.2. Scaled concentration maps

Once the slope errors have been estimated, the concentration ratio of flux density ( $C_F$ ) of each heliostat is quantified. This concentration is the ratio between the incident flux density and the instantaneous direct normal irradiation ( $DNI$ ); Eq. (2). Thus,  $C_F$  is interpreted as the number of "suns" impinging on each point of the target,

$$C_F = \frac{F}{DNI} \quad (2)$$

To scale the original experimental images from normalized to absolute concentration ratio, the model is again utilized. The flux maps of absolute concentration are generated by the model, considering the optical losses: cosine, mirror reflectivity (94%), and atmospheric attenuation (Leary and Hankins correlation).

The total energy intercepted by the 2x2 m<sup>2</sup> target must be the same as that simulated by the model. On the basis of this assumption, the experimental normalized image is transformed into absolute concentration ratios as affected by a scaling factor; Eq. (3). Such a scaling factor ( $SCL$ ) is computed with Eq. (4), where  $dA$  is the area of each pixel,

$$C_{F,exp} = SCL \cdot C_{N,exp} \quad (3)$$

$$SCL = \frac{\sum(C_F \cdot dA)_{mod}}{\sum(C_N \cdot dA)_{exp}} \quad (4)$$

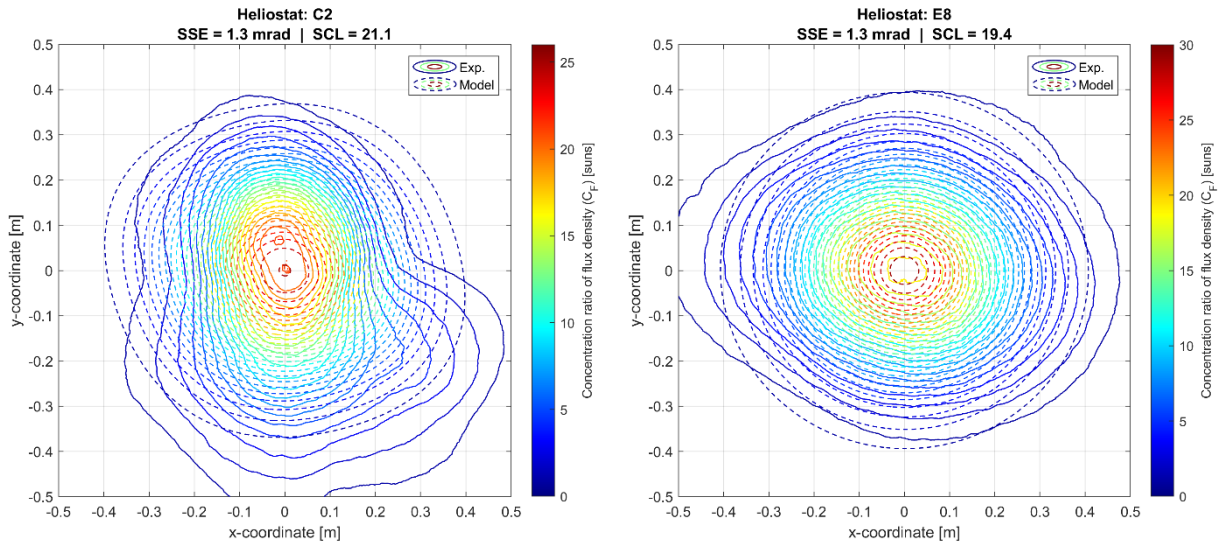


**Figure 3.** Concentration ratio of flux density for heliostats C2 and E8. Experimental (solid) vs. model (dotted) contours.

For heliostats C2 and E8, Figure 3 shows the flux maps of concentration ratio both from the model (dotted) and experimental measurements (solid contours). The experimental contours have been transformed to absolute concentration ratios of flux density using the resulting  $SCL$  factors.

## 4. Uniform aiming

Uniform flux distributions on the receiver minimize the thermal stresses and fatigue. This section presents first the aiming strategy for circular aperture receivers and, secondly, the optimization carried out for PROTEAS.

### 4.1 Aiming strategy

The so-called Blossaim strategy relies on the principle of aiming each heliostat so that the beam is tangent to the receiver aperture edge. Let  $r_{app}$  and  $r_{beam}$  respectively be the radius of the aperture and the beam, the aim point is positioned at a distance  $r_{app} - r_{beam}$  from the center and at an angular position  $\theta_{aim}$ , as shown in Fig. 4 (left). The beam radius is determined as a function of the aiming factor  $k$ , according to Eq. (5), where  $D$  stands for the heliostat-to-target distance and  $\sigma_e$  is the effective error computed with Eq. (6); with  $\omega$  being the heliostat incidence angle and the sun image is  $\sigma_{sun}=2.09$  mrad:

$$r_{beam}=k \cdot D \cdot \sigma_e, \quad (5)$$

$$\sigma_e=\sqrt{\sigma_{sun}^2+2(1+\cos^2 \omega)SSE^2}. \quad (6)$$

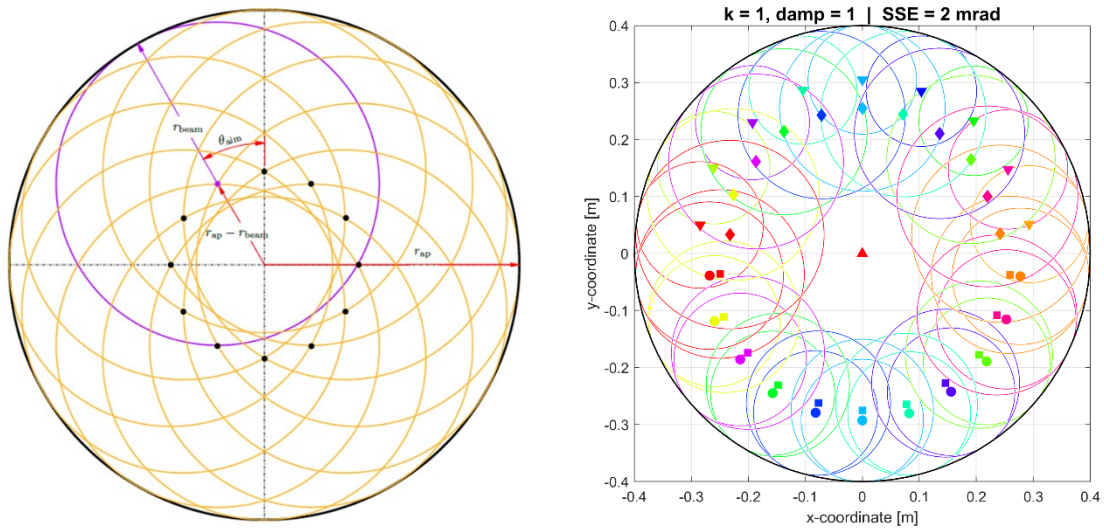


**Figure 4.** Aim point positioning in the Blossaim strategy (left). Aim points for  $k = 1$  and  $SSE = 2$  mrad in all heliostats (right).

For the angular positioning, the following deterministic procedure was selected for the PROTEAS field. The first and fourth rows (A and D) aim at the upper half and the second and third (B and C) at the bottom, while last E row aim at the center. Thus, the procedure assumes that all heliostats are aiming at the receiver, neglecting events like heliostats going offline.

For  $k=1$  and assuming a constant  $SSE=2$  mrad, Figure 4 (right) shows the aim points, where each heliostat is identified according to the markers in the Fig. 1 layout (right). As can be inspected from Fig. 4 (right), the heliostats in a row are alternatively aimed at the left (East) and right (West) sides of the receiver. This way, fairly symmetric flux maps are obtained throughout the day, without significantly altering the position of the aim points. To avoid larger peaks in the horizontal axis of the receiver, the Blossaim implementation introduced a damping factor (smaller than 1), to bias  $\theta_{aim}$  towards the vertical axis. Further detail on the damping factor, and the Blossaim strategy, can be found in Ref. [8].

In summary, the aiming strategy for a circular aperture receiver is controlled by two parameters:  $k$  and *damping*. The central symmetry is regulated with the damping factor, while the  $k$  factor affects to the concentration and spillage. For a constant  $damp=0.8$ , Fig. 5 shows the aim points (top) and flux distributions (bottom) for  $k$  factors of 2.0, 1.5, 1.0 and 0.5 in PROTEAS. The smaller the  $k$  is, the lower the peak becomes, at the expense of increasing the spillage losses. For proper comparison the color axis of concentration ratio is kept constant in Fig. 5.

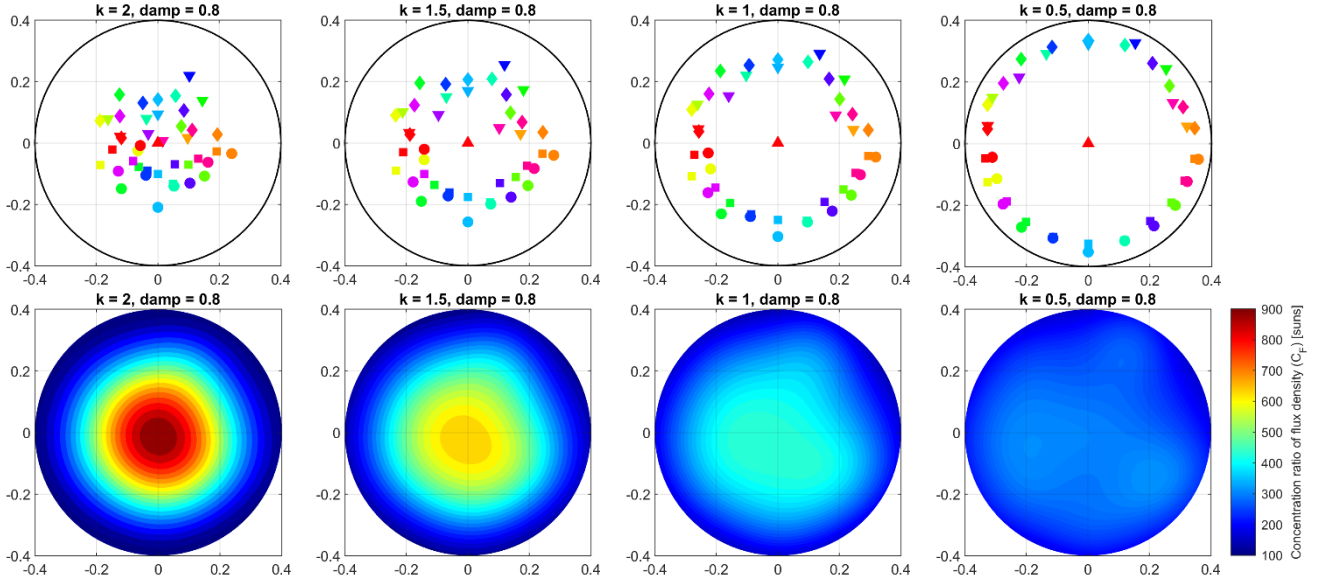


**Figure 5.** Maps of aim points (top) and flux concentration (bottom) for decreasing values of  $k$  aiming factor: 2.0, 1.5, 1.0 and 0.5 ( $damp = 0.8$ ).

## 4.2 Optimization

The ideal combination of  $k$  and *damping* factor leading to the most uniform flux distribution is explored in this subsection. To quantify the flux homogeneity, two objective functions are used: the coefficient of variation and the spillage loss.

The coefficient of variation ( $CV$ ) is a measure of the non-uniformity of the flux distribution, as previously utilized by Wang et al. [3]. It is the ratio of the standard deviation to the mean. For the concentration ratio of flux density ( $C_F$ ) in a mesh with  $N_{el}$  elements (or pixels) the  $CV$  is computed with Eq. (7). The  $CV$  can be expressed as a percentage, so that values towards 0% reveal high uniformity:

$$CV = \frac{\sqrt{\frac{\sum_{i=1}^{N_{el}} (C_{F,i} - \bar{C}_F)^2}{N_{el} - 1}}}{\bar{C}_F} \quad (7)$$

However, a fully flat distribution may only be achievable without using the heliostats (null interception). To trade off with the  $CV$ , the spillage loss ( $SPL$ ) must be controlled too. According to Eq. (8),  $SPL$  is a percentage so that 0% means no spillage loss. The intercept factor ( $f_{int}$ ) is computed by FluxSPT:

$$SPL = 1 - f_{int} \quad (8)$$

The goal of the optimization is to minimize both the  $CV$  and the  $SPL$ . For PROTEAS, an exhaustive search has been performed with  $k$  factors ranging from 0.5 to 2.0 in 0.1 steps and *damping* factors ranging from 0.5 to 1.0 in 0.05 steps. For all these combinations, Fig. 6 shows the resulting coefficients of variation (horizontal axis) and spillage losses (vertical). As

expected, the smaller the  $k$  factor is, the lower the CV but the higher the SPL becomes, and the other way round. The damping factor does not significantly affect the SPL and the smallest CV is obtained with a *damping* factor of around 0.85. The Pareto optimal solution is the one closest to CV=0 and SPL=0.

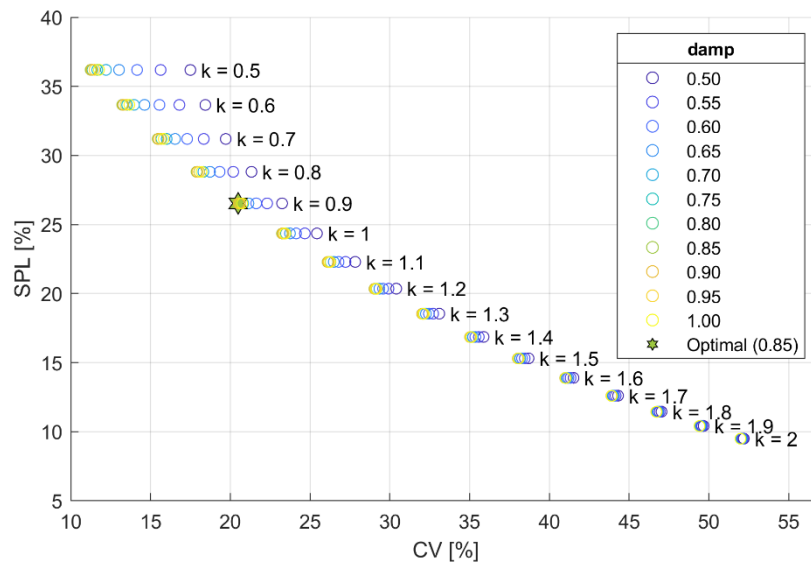


**Figure 6.** Search space. Representation of the coefficient of variation (CV) and the spillage loss (SPL) for the different pairs of  $k$  and *damping* factors.

From the optimization, the most uniform flux distribution is expected with an aiming factor equal to 0.9 and a damping factor of 0.85 (marked with a star symbol in Fig. 6). With these parameters, the resulting aim points are shown in Fig. 7 (left). Using these aim points, the map of flux density concentration ratio on the aperture is shown in Fig. 7 (right), where a flat region emerges in the center (slightly biased to bottom-left).

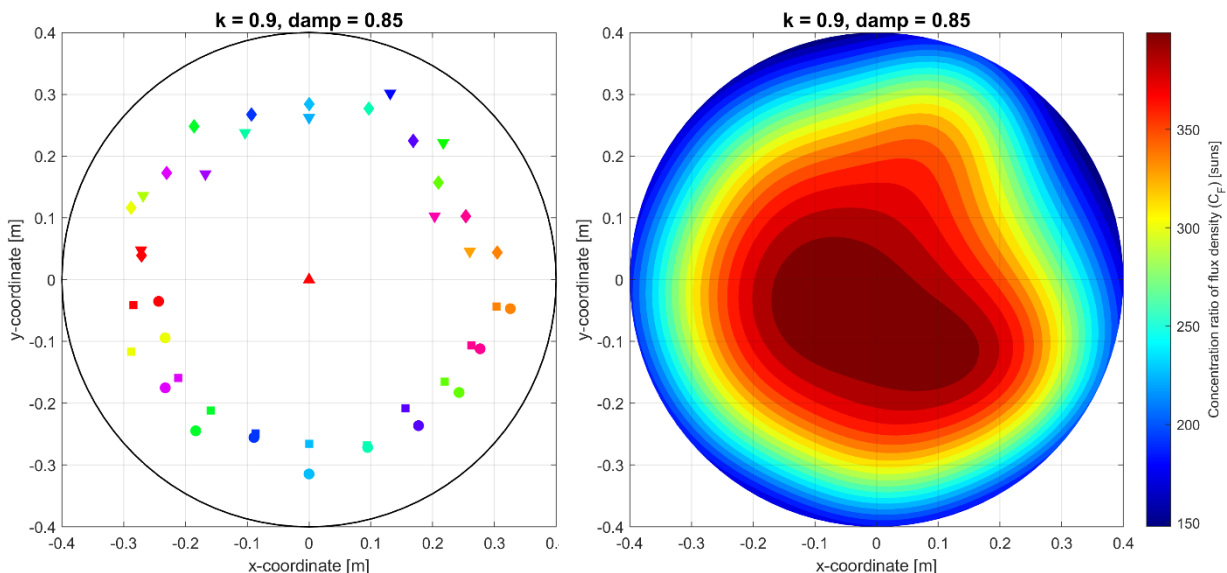


**Figure 7.** Aim points for each heliostat (symbols and color according to Fig. 1, right) for the optimum aiming:  $k=0.9$  and  $damp=0.85$  (left). Flux distribution by the model (right).

## 5. Experimental validation

The aiming strategy is validated by comparing the modeled and the experimental flux distributions. The scaled experimental maps obtained in subsection 3.2 are superimposed using

the optimum aim points found in the previous section. Thereby, the synthetic flux map shown in Fig. 8 (left) is generated, again with a flat central region.

The contour plot in Fig. 8 (right) represents both the synthetic (solid lines) and the modeled (dashed) flux maps. As displayed on the top, the cross-correlation coefficient between both distributions is as high as 96.3%. The peak concentration ratio is overestimated by the model (411.8) in comparison with the experimental image (366.5). This may be attributed to the non-constant slope error of the heliostats as well as their astigmatic aberrations, not already accounted for by the model. However, the uniformity of both distributions is fairly similar, with coefficient of variation of 20.5% and 22.8%, respectively for the model and experimental measurements.

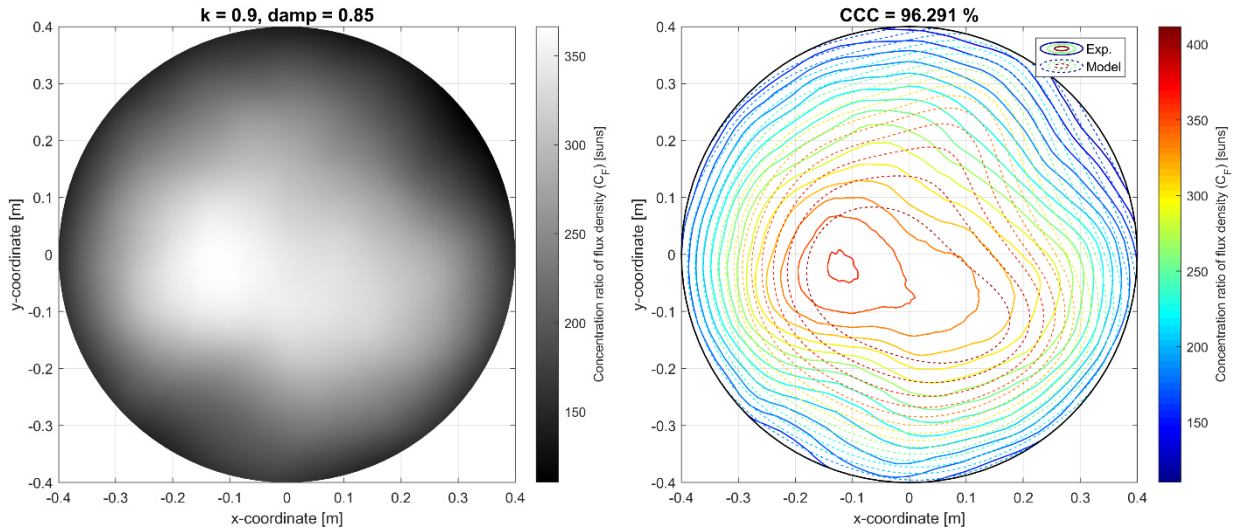


**Figure 8.** Experimental synthetic flux distribution (left) and comparison with the model (right) for the optimized uniform aiming.

The improvement of optimized aiming is shown by contrasting the results with single point aiming. As displayed in Table 2, the peak concentration ratio is reduced from 1090 (single aiming) to 366.5. Similarly, the non-uniformity (CV) is decreased from 70% to 22.8%, so that the thermal stresses in the receiver can be correspondingly reduced. This benefit is obtained by increasing the spillage losses by 21.8 percentage points (from 4.7% to 26.5%), according to the model's results.

**Table 2.** Performance indicators for single and optimized aiming, both by the model and the experiments.

| Aiming                                 |       | $C_{F,max}$ [-] | $C_{F,mean}$ [-] | CV [%] | SPL [%] |
|--|-------|-----------------|------------------|--------|---------|
| Optimized<br>( $k=0.9$ , $damp=0.85$ ) | Model | 411.8           | 343.4            | 20.49  | 26.53   |
|  | Exp.  | 366.5           | 281.0            | 22.82  |         |
| Single                                 | Model | 1453.4          | 676.4            | 72.28  | 4.71    |
|  | Exp.  | 1090.2          | 517.5            | 69.97  |         |

## 6. Conclusions

An experimental campaign has been carried out at the PROTEAS field to develop and validate an aiming strategy. Experimental images have been taken for the 50 heliostats, and their slope errors have been estimated by means of a fitting process using the FluxSPT convolution-projection model. The experimental images have been rescaled to provide flux maps of the concentration ratio.

The Blossaim aiming strategy has been applied to the PROTEAS field with a circular aperture receiver. This deterministic strategy relies on aiming the heliostats so that their beams are tangent to the aperture edge. To control the distribution of aim points, two parameters are utilized: an aiming factor ( $k$ ) and a damping factor.

A uniform flux distribution has been searched with the aiming strategy. This has been achieved by minimizing both the coefficient of variation and the spillage losses. As a result, the combination of  $k=0.9$  and  $damp=0.85$  has led to the most homogeneous distribution, so as to reduce receiver thermal stresses and fatigue.

With the resulting aim points, the flux maps of concentration ratio have been generated both by the model and synthetically with the experimental images. The cross-correlation between them is as high as 96%, showing the validity of the modeling, even though the model slightly overestimates the local concentration ratios.

Compared to single point aiming, optimized aiming reduces the peak concentration from 1090 to 367 suns, as well as the non-uniformity coefficient of variation from 72% to 20%, according to the synthetic flux maps. On the contrary, the spillage loss necessarily increases by 21.8 percentage points according to the model.

Future actions involve the commissioning of the moving target in front of the receiver aperture. With this cooled target, all heliostats can be aimed simultaneously, eliminating the step of synthetic generation of experimental maps. At the same time, the flux meter included in the moving target allows to straightforwardly rescale the flux maps. The 3D shape of a receiver like iSTORE, as opposed to the flat surface, is another line of research.

## Author contributions

**A. Sánchez-González:** Conceptualization, Methodology, Software, Validation, Visualization, Writing – original draft, Funding acquisition. **D.J. Erasmus:** Methodology, Writing – review & editing. **M.C. Georgiou:** Project administration, Writing – review & editing.

## Competing interests

The authors declare no competing interests.

## Funding

SFERA-III project (Grant Agreement No. 823802).  
Spanish government under the project PID2019-109224RA-I00.

## Acknowledgement

We thank The Cyprus Institute for providing access to its installations, and the support of its scientific and technical staff.

## References

1. W. R. Logie, J. D. Pye, and J. Coventry, "Thermoelastic stress in concentrating solar receiver tubes: A retrospect on stress analysis methodology, and comparison of salt and sodium," *Sol. Energy*, vol. 160, no. November 2017, pp. 368–379, 2018, doi: <https://doi.org/10.1016/j.solener.2017.12.003>.
2. S. M. Besarati, D. Yogi Goswami, and E. K. Stefanakos, "Optimal heliostat aiming

- strategy for uniform distribution of heat flux on the receiver of a solar power tower plant," *Energy Convers. Manag.*, vol. 84, pp. 234–243, Aug. 2014, doi: <https://doi.org/10.1016/j.enconman.2014.04.030>.
3. K. Wang, Y.-L. He, X.-D. Xue, and B.-C. Du, "Multi-objective optimization of the aiming strategy for the solar power tower with a cavity receiver by using the non-dominated sorting genetic algorithm," *Appl. Energy*, vol. 205, pp. 399–416, Nov. 2017, doi: <https://doi.org/10.1016/j.apenergy.2017.07.096>.
  4. M. Watkins, M. Wagner, J. Hinze, S. Sullivan, E. Vollnogle, and J. Boxleitner, "Heliostat aiming strategies for arbitrary flux profiles for high temperature gas-based receivers," in *SolarPACES 2019, 2020*, p. 160008, doi: <https://doi.org/10.1063/5.0032149>.
  5. A. Sánchez-González, M. R. Rodríguez-Sánchez, and D. Santana, "Aiming factor to flatten the flux distribution on cylindrical receivers," *Energy*, vol. 153, pp. 113–125, Jun. 2018, doi: <https://doi.org/10.1016/j.energy.2018.04.002>.
  6. M. J. Wagner and T. Wendelin, "SolarPILOT: A power tower solar field layout and characterization tool," *Sol. Energy*, vol. 171, pp. 185–196, Sep. 2018, doi: <https://doi.org/10.1016/j.solener.2018.06.063>.
  7. A. Sánchez-González, M. R. Rodríguez-Sánchez, and D. Santana, "FluxSPT: Tool for heliostat field aiming and flux mapping in solar power tower plants," in *SolarPaces 2020, 2022*, p. 120020, doi: <https://doi.org/10.1063/5.0085656>.
  8. D. J. Erasmus, A. Sánchez-González, and T. W. von Backström, "Blossaim, a deterministic aiming strategy for circular aperture receivers," in *SolarPACES 2020, 2022*, p. 120012, doi: <https://doi.org/10.1063/5.0085654>.
  9. K. G. Stokos et al., "The control system at PROTEAS," in *SolarPACES 2017, 2018*, vol. 2033, p. 210019, doi: <https://doi.org/10.1063/1.5067221>.
  10. C. N. Papanicolas et al., "CSP cogeneration of electricity and desalinated water at the Pentakomo field facility," in *SolarPACES 2015, 2016*, p. 100008, doi: <https://doi.org/10.1063/1.4949196>.